

# Materials Advances

Accepted Manuscript

This article can be cited before page numbers have been issued, to do this please use: T. Gross, J. Wu, R. Yongsunthon, J. J. Price, R. Yougman, K. Singh, B. D. Fulmer and J. Jones, *Mater. Adv.*, 2026, DOI: 10.1039/D6MA00421K.



This is an Accepted Manuscript, which has been through the Royal Society of Chemistry peer review process and has been accepted for publication.

Accepted Manuscripts are published online shortly after acceptance, before technical editing, formatting and proof reading. Using this free service, authors can make their results available to the community, in citable form, before we publish the edited article. We will replace this Accepted Manuscript with the edited and formatted Advance Article as soon as it is available.

You can find more information about Accepted Manuscripts in the [Information for Authors](#).

Please note that technical editing may introduce minor changes to the text and/or graphics, which may alter content. The journal's standard [Terms & Conditions](#) and the [Ethical guidelines](#) still apply. In no event shall the Royal Society of Chemistry be held responsible for any errors or omissions in this Accepted Manuscript or any consequences arising from the use of any information it contains.

## 1 Indentation of glasses that produce a boundary-forming annular crack

2 TM Gross<sup>1</sup>, J Wu<sup>1</sup>, R Yongsunthon<sup>1</sup>, JJ Price<sup>1</sup>, RE Youngman<sup>1</sup>, K Singh<sup>1</sup>, BD Fulmer<sup>1</sup>, J Jones<sup>1</sup>

3 <sup>1</sup>Science and Technology, Corning Research and Development Corporation, Painted Post, New  
4 York 14870, USA

### 5 Correspondence

6 Timothy M. Gross, Science and Technology, Corning Research and Development Corporation,  
7 Painted Post, New York, 14870, USA

8 Email: grosstm@corning.com

### 9 Abstract

10 A series of boroaluminosilicate glasses is designed that spans the range of Vickers indentation  
11 cracking behaviors. At one endpoint, median/radial cracking is observed, whereas the other  
12 endpoint exhibits ring and cone cracking. In the transition in cracking behavior across the glass  
13 series, a composition space is identified that produces a large boundary-forming annular crack  
14 that prevents the extension of radial cracks emanating from the indent impression. Indentation  
15 cross-sectioning shows that this unique cracking system forms as a traditional cone crack which  
16 is then redirected back to the surface following unloading by residual stress. The percentage of  
17 volume displaced from 30 mN Berkovich scratch grooves was 10-15% for glasses that produce  
18 the annular crack. This places this new glass space on the anomalous end of the deformation  
19 continuum, but with more volume-conserving shear component than fully anomalous glass like  
20 silica. This unique combination of densification and shear enables formation of the initial cone  
21 crack (densification contribution) and provides the residual stress (shear contribution) that causes  
22 the cone crack to be redirected back to the surface. Retardance measurements through the cross-  
23 section show that residual stresses initially associated with lateral crack extension interact with  
24 cone crack to drive it back to the surface.

### 25 Introduction

26 Indentation deformation and cracking of glasses has been studied extensively, with much of the  
27 historical work limited to commercially available soda-lime silicate and silica<sup>1-8</sup>. Conveniently,  
28 these glass types serve as extreme endpoints in the Vickers indentation response spectrum.  
29 Soda-lime silicate glass, categorized as a normal glass, deforms with a significant volume-  
30 conserving shear contribution<sup>2-5,7-10</sup>. The displaced volume results in glass pile-up in the region  
31 surrounding the indent periphery. Shear readily initiates at weak points in the glass network  
32 associated with non-bridging oxygens (NBO)<sup>2-3</sup>. Shear faults in the subsurface act as starter  
33 cracks for larger median/radial and lateral cracking systems that appear a modest applied  
34 indentation loads<sup>4-5,7-8</sup>. On the other hand, silica, categorized as anomalous glass, deforms  
35 primarily by volume-reducing densification<sup>1-2,5,8-11</sup>. The high connectivity of the essentially  
36 NBO-free, tetrahedral network is more resistant to shear deformation<sup>9</sup>. Deformation by  
37 densification results in high tensile stresses at the surface during loading, thus leading to ring  
38 cracking at the indent periphery at low applied loads<sup>6,8-9,12</sup>. More recently, a third category of



1 glasses was appropriately defined as intermediate, since these glasses deform with more  
2 densification than normal soda-lime glass and more shear than anomalous silica glass<sup>9,13</sup>.  
3 Examples explored thus far in this category are also essentially NBO-free, but incorporation of  
4 trigonal boron into the silicate network reduces the average coordination of glass formers. This  
5 less rigidly constrained network enables greater shear when compared to silica, alleviating ring  
6 cracking stresses<sup>12-13</sup>. Still, the network is well connected, so densification remains high when  
7 compared to soda-lime silicate and the resulting sub-surface damage is minimal<sup>9,13</sup>. Trigonal  
8 boron enables both shear and densification, shear from the less constrained network and  
9 densification from the transition from trigonal to tetrahedral coordination under pressure<sup>14-15</sup>. In  
10 a subset of intermediate glasses with high trigonal boron content, high indentation crack  
11 resistance is achieved through delocalized shear deformation that enables displacement without  
12 shear faulting<sup>9</sup>.

13 Berkovich nanoscratch experiments have recently been used to characterize the amount of shear  
14 displacement in various glass types, thus providing a straight-forward means of defining glasses  
15 as normal, anomalous, or intermediate<sup>9</sup>. While the Vickers tip is commonly used in large  
16 impression micro-indentation testing, the Berkovich tip is used in nano-scratch experiments  
17 where the tip of the indenter has a considerable influence on the deformation. The precision  
18 radius at the apex of the three-sided Berkovich tip is preferred over the variable junction-offset  
19 present in four-sided Vickers tips for nano-indentation and nano-scratch studies. Since the  
20 Berkovich and Vickers tips provide the same contact area to indentation depth ratio, they may be  
21 used interchangeably, with preference depending on the loading regime. The volume displaced  
22 by shear into the pile-up regions for a 30 mN Berkovich scratch is approximately 30% for  
23 intermediate glasses, whereas normal soda-lime silicate and anomalous silica have displaced  
24 volumes of 50% and 9%, respectively<sup>9</sup>.

25 The establishment of intermediate glasses demonstrates that the indentation response of glasses  
26 is a continuum between the well-known end-point glasses, those defined as normal and  
27 anomalous. It is also not satisfactory to simply place all glasses in one of these three buckets.  
28 Along the transition in indentation response behavior, we encounter glasses that have their own  
29 unique characteristics. The present study highlights a borosilicate composition window near the  
30 anomalous end of the spectrum that forms a unique annular crack with a diameter several times  
31 larger than the indentation major diagonal length<sup>16,17</sup>. Due to its ability to act as a boundary  
32 against the extension of strength-limiting radial cracks, it is referred to as a “boundary-forming  
33 annular crack” in the present work.

34

## 35 **Experimental**

### 36 **Glass sample preparation**

37 A series of sodium boroaluminosilicate glasses was prepared from sand (Puresil 100C-1; Sibelco  
38 Bao Lin Co., Ltd.), calcined alumina (A-2 unground; Almatix, Inc.), boric acid (technical grade;  
39 Chemical Distributors Inc.), and sodium carbonate (soda ash grade 260; Amrex Chemical Co.,  
40 Inc.). For each glass composition, 2 kilograms (kg) of the batch was mixed in a Turbula mixer



1 for 15 minutes, then melted at 1650°C for 12 h in a covered platinum crucible. The molten  
2 glasses were poured onto a clean, stainless-steel table and transferred to annealing furnaces set to  
3 600°C. Glasses were annealed for 8 h and cooled in the furnace at a rate of 100°C/h. The  
4 compositions were analyzed by x-ray fluorescence (XRF) and B<sub>2</sub>O<sub>3</sub> content was determined by  
5 inductively coupled plasma - optical emission spectroscopy (ICP-OES). Samples for mechanical  
6 testing were prepared into testing coupons with dimensions of 50 x 50 x 1 mm. The surfaces of  
7 the samples were ground using 150 and 320 grit resin bonded diamond in water. The surface  
8 was then polished to an optical finish using 22 μm Al<sub>2</sub>O<sub>3</sub> in water followed by a cerium oxide  
9 and water slurry. Specimens of commercially available, fusion-drawn Corning® Fusion5® at 1  
10 mm thickness were also used for mechanical testing. Samples were prepared as 50 x 50 mm  
11 coupons by a scribe and break process.

12 To demonstrate the role of fictive temperature on boundary-forming annular crack formation,  
13 select specimens were heat-treated to set the fictive temperatures equal to the strain pt, anneal pt,  
14 and 10<sup>10</sup> Pa·s temperatures. To ensure full relaxation to the specified fictive temperature,  
15 specimens were heat-treated at times significantly longer than estimated minimum structural  
16 relaxation time of 30τ, where the relaxation time, τ, is equal to η/G. The value to η is the  
17 viscosity at the specified fictive temperature target, i.e., 10<sup>13.68</sup> Pa·s for the strain pt and 10<sup>12.18</sup>  
18 Pa·s for the anneal pt. The value for shear modulus, G, is taken from the resonant ultrasound  
19 spectroscopy (RUS) data at room temperature and in the as-annealed state. The lower G values  
20 at the fictive temperatures of interest further justify the additional heat-treatment times well  
21 beyond 30τ. Heat treatment at the strain point was conducted for a duration of one week, heat  
22 treatment at the anneal point was conducted for 4 hours, and heat treatment at 10<sup>10</sup> Pa·s was  
23 conducted for 10 minutes. A gentle fan cool was appropriate to lock in the fictive temperatures  
24 for samples heat treated at the strain and anneal points due to their lengthy relaxation times. For  
25 the sample heat treated at 10<sup>10</sup> Pa s, the specimen was quickly removed from the furnace and  
26 placed into an air quenching apparatus consisting of three high velocity fans to lock in the fictive  
27 temperature to as close to the target as possible.

## 28 **Physical property measurement**

29 Physical property measurements were made on the prepared glass compositions including  
30 density measurement by buoyancy method<sup>18</sup>, coefficient of thermal expansion (CTE)  
31 measurement from 25-300°C by dilatometry<sup>19</sup>, strain and anneal point determination by beam  
32 bending viscosity (BBV)<sup>20</sup>, softening point measurement by parallel plate viscosity (PPV)<sup>21</sup>, and  
33 measurement of elastic properties via resonant ultrasound spectroscopy (RUS)<sup>22</sup>. Refractive  
34 index at 589.6 nm was measured using an Abbe refractometer<sup>23</sup>. The 10<sup>10</sup> Pa s temperature was  
35 estimated for each of the crucible melted glasses by fitting a Fulcher curve through the strain,  
36 anneal, and softening points. The 10<sup>10</sup> Pa s temperature is representative of the fictive  
37 temperature of fusion-formed glass<sup>24</sup>.

## 38 **Structural Characterization**

39 <sup>11</sup>B MAS NMR experiments were conducted with a commercial spectrometer (Agilent DD2) and  
40 a 16.4 T narrow-bore superconducting magnet. The resonance frequency of <sup>11</sup>B at this magnetic



1 field was 224.52 MHz. Samples were powdered using an agate mortar and pestle and packed into  
2 3.2 mm outer diameter zirconia rotors, with sample spinning controlled to  $20 \pm 0.001$  kHz. 200–  
3 1000 scans were co-added for each sample, making use of  $0.6 \mu\text{s}$  radio-frequency pulse widths  
4 ( $\pi/12$  tip angle) and a recycle delay of 10 s between scans. Data were processed using  
5 commercial software and without any apodization. The  $^{11}\text{B}$  MAS NMR spectra were frequency  
6 referenced using a secondary shift reference (aqueous boric acid) at 19.6 ppm relative to the  
7 standard boron trifluoride etherate  $\text{BF}_3\text{O}(\text{Et})_2$  reference. Spectra were deconvoluted using  
8 DMFit<sup>25-26</sup>, with the “Q mas  $\frac{1}{2}$ ” model representing the 2nd-order quadrupolar broadened  
9 lineshapes of the trigonal boron resonances, and the “Gaus/Lor” model approximating the  
10 tetrahedral boron lineshapes. Determination of  $N_4$  (the ratio of four-coordinated to total boron)  
11 was made by integrating the areas of these peaks, and with consideration of  
12 spinning sidebands and a strongly overlapping contribution from the satellite transitions of the  
13 four-coordinated boron<sup>27</sup>.

#### 14 Mechanical testing

15 Vickers indentation was performed at 25°C and 50% relative humidity using a LECO LV800AT  
16 macrohardness tester with a dwell time fixed at 10 s. Loading and unloading rates were  
17 displacement controlled at  $60 \mu\text{m/s}$ . Optical imaging of the surface view of indents was  
18 performed 5 minutes after indentation. An indentation cross-section of a Fusion5® specimen  
19 exhibiting the boundary forming annular crack was prepared using the technique developed by  
20 Hagan<sup>6-7</sup>. The LECO LV800AT Vickers hardness tester was used to make the indents at the tip  
21 of a pre-crack. The pre-crack is created by initially making an indent at 10 kilograms force  
22 (kgf). The 10 kgf load is high enough to produce radial cracks that can be propagated by  
23 bending the glass specimen by hand. Manual bending is used to extend the pre-crack by at least  
24 10 major diagonal lengths of the 10 kgf indent. One major diagonal of the indent impression was  
25 aligned with the pre-crack, so when fracturing the sample, the indents would be bisected into two  
26 halves for analysis. Indent surface and cross-section images were captured using a Nikon  
27 Eclipse ME600 compound optical microscope with polarized light.

28 To demonstrate the boundary-forming capability of the annular crack, a 1mm thick Fusion5®  
29 specimen was indented at 2 kgf then placed on a hot plate at 130°C. After 5 minutes, ice water  
30 was dropped onto the indent location. Images of the radial cracks before and after thermal shock  
31 were captured with the compound optical microscope.

32 Scratches were made in the  $\text{Na}_2\text{O}\cdot\text{Al}_2\text{O}_3\cdot\text{B}_2\text{O}_3\cdot\text{SiO}_2$  (NABS) and Fusion5® glasses with a  
33 Berkovich tip at a constant load of 30 mN using an MTS Nano G200 nanoindenter. A lateral  
34 edge of the indenter was pointed forward when conducting scratches. The 30 mN load was  
35 selected since higher loads produced significant machine curling of pile-up material, thus making  
36 subsequent pile-up measurements difficult. The scratch impression area and pile-up areas were  
37 measured using atomic force microscopy (AFM). The AFM scans were performed on a Bruker  
38 Bioscope Catalyst in tapping mode using TESP probes. The substrates were manually positioned  
39 such that the scratches were perpendicular to the fast scan (horizontal) axis, to ensure that any tip  
40 geometric convolution effects would be consistent across all samples. Slow scan rates, low  
41 feedback gains, and moderate tapping setpoints were used to minimize “overshoot” artifacts at



1 the pileup regions and optimize topographic accuracy. The scratches were centered relative to  
2 the scan region and the scans were flattened with a second order polynomial fit to flat (control)  
3 regions on both sides of the scratches. MATLAB was used to calculate the scratch and pileup  
4 areas for every scan line (row) of the 512x512 pixel height images. The averages were  
5 calculated from values extracted across all rows in an image, only excluding anomalous scan  
6 lines. The uncertainties quoted for all extracted parameters represent true variability of the  
7 calculated areas, not instrumental error. The variability of the area calculations is mostly due to  
8 real variability of the scratch topography, however, some of it can be attributed to polishing  
9 flaws on the substrate surfaces. Since the pile-up is consistent along the scratch track, we may  
10 interchangeably refer to displaced material as % displaced area or % displaced volume.

### 11 Retardance measurement

12 An experimental setup was prepared to measure the evolution of the stress field during the  
13 formation of annular ring cracks. The in situ photoelastic measurement apparatus was built  
14 around the LV800AT LECO Vickers Hardness Tester. Retardation measurements were taken  
15 through cross-sections of indents made at 3 kgf with a 10 s dwell time. Measurements were taken  
16 immediately after unloading, then again at 750 ms, 8s, and 12 s. An illumination module was  
17 constructed with a Thorlabs M530L4 530 nm LED, diffuser (D), linear polarizer (LP), quarter-  
18 wave plate (QWP) and 25.4 mm focal length collimation lens (CL) producing uniform  
19 collimated right-circularly polarized illumination through an optically polished 10 mm × 5 mm  
20 × 3 mm Fusion5® specimen. Spatially resolved Stokes intensity measurements were captured  
21 using an imaging module comprised of a telecentric relay system. This relay system imaged the  
22 plane of the indent onto the focus of a Newport M-20X objective lens (OL) which was used to  
23 magnify the image onto the sensor of a LUCID Vision Labs PHX050S1-PC Polarization camera  
24 (PC) operating at ~20 fps. The camera sensor simultaneously captures all four required intensity  
25 projections and images are post processed to extract the integrated retardance and slow-axis  
26 angles from the measurement of the  $S_1$  and  $S_2$  Stokes parameters of the output light<sup>28</sup>. A  
27 schematic of the experimental system is shown in Fig. 1.

### 28 Results

29 The batched and analyzed compositions for the NABS crucible melted glasses are given in Table  
30 I. The series is designed such that  $B_2O_3$  is increased at the expense of  $Na_2O$  when going from  
31 NABS-1 to NABS-4. A brief description of the structural role of  $Na^+$  is important to understand  
32 the transition from NABS-1 to NABS-4. In general,  $Na^+$  is first consumed in the role of charge  
33 balancing  $Al^{3+}$  and thus allows it to substitute into  $Si^{4+}$  positions in the tetrahedral network of the  
34 glass. Once  $Al^{3+}$  ions that are present are charge compensated,  $Na^+$  will next charge compensate  
35  $B^{3+}$  such that it can also substitute for  $Si^{4+}$  in tetrahedral positions<sup>29</sup>. The remaining  $Na^+$  in  
36 excess of both  $Al^{3+}$  and  $B^{3+}$  modifies the glass network by creating non-bridging oxygens.

37 As shown in the  $^{11}B$  NMR spectrum in Fig. 2a, the percentage of boron in tetrahedral  
38 coordination is 91.2% for NABS-1. Since NBAS-1 has 9.5 mol%  $Na_2O$  in excess of the sum of  
39  $Al_2O_3$  and  $B_2O_3$ , the glass has considerable non-bridging oxygens (NBOs) making this glass the  
40 most “normal” of the NABS series. Non-bridging oxygens reduce connectivity and break the



1 ring structures such that the network may be thought of as partially collapsed. The highest  
2 density value ( $2.428 \text{ g/cm}^3$ ) of the series results from this NBO-rich, collapsed network  
3 containing a high concentration of space filling  $\text{Na}^+$  ions.

4 Moving across the series to NABS-2, the  $\text{B}_2\text{O}_3$  is increased at the expense of  $\text{Na}_2\text{O}$  to make  
5  $\text{Na}_2\text{O}$  nearly equal to  $(\text{Al}_2\text{O}_3 + \text{B}_2\text{O}_3)$ . This charge balanced composition without excess  $\text{Na}^+$  has  
6 limited NBOs and a high concentration of tetrahedral boron as shown in Fig. 2a ( $N_4 = 74.7\%$ ).  
7 This glass has the lowest Poisson's ratio in the series, thus indicating the highest degree of  
8 covalency, i.e. a high degree of tetrahedral coordination with few NBOs. This high degree of  
9 network connectivity leads to the highest values for strain and anneal points as well as the  
10 highest values for elastic moduli.

11 Next, the NABS-3 composition has  $(\text{Al}_2\text{O}_3 + \text{B}_2\text{O}_3)$  greater than  $\text{Na}_2\text{O}$  by 9.95 mol%, so the  
12 glass is free of NBOs and without nearly enough  $\text{Na}^+$  to charge compensate  $\text{B}^{3+}$ , the glass now  
13 has considerable fraction of trigonal boron. As shown in Fig. 2a,  $N_3$  is 66.9% while  $N_4$  decreases  
14 to 33.1%.

15 The final glass in the series, NBAS-4, has  $\text{Na}_2\text{O}$  slightly in excess of  $\text{Al}_2\text{O}_3$ , so the glass is NBO-  
16 free and essentially all of the boron is present as  $N_3$  as shown in Fig 2a. With very little  $\text{Na}_2\text{O}$   
17 content, the glass is made up of almost all glass-forming oxides. With few space filling modifier  
18 ions, the glass has the lowest density and is considered the most anomalous of the glasses in the  
19 series.

20 Table II provides the properties of commercially available Corning® Fusion5® glass. This glass  
21 is a version of NABS-3 that was modified to optimize manufacturability and to tune in the  
22 attributes required for a windshield glass application. Structurally, this glass may be considered  
23 a close cousin to NABS-3. The Fusion5® composition is proprietary and includes other  
24 modifier ions besides  $\text{Na}^+$ . In table II, the term  $R_x\text{O}$  is defined as the sum of alkali and alkaline  
25 earth oxides. A comparison of the properties shown in Tables I and II for NABS-3 and Fusion5,  
26 respectively, reveals similar properties with the notable exception of the softening pt. This  
27 property was specifically tailored to obtain the desired sagging temperature for Fusion5® in the  
28 windshield forming operation.

29 The  $^{11}\text{B}$  NMR spectra in Fig. 2a also shows that the  $\text{BO}_4$  peak shifts to the left when going across  
30 the series from NABS-1 to NABS-4. The peak centered at approximately -2 ppm is  
31 representative of B surrounded by four Si ions<sup>30</sup>. The peak centered at approximately 0 ppm  
32 represents B surrounded by 2 to 3 Si ions and 1 to 2 B ions<sup>30</sup>. This interpretation is consistent  
33 with the concentration of B increasing substantially across the series.

34 Vickers indents are shown in Fig. 3 for glasses in the NABS series at 1 and 2 kgf. Each glass  
35 was heat-treated to set the fictive temperature to the respective anneal pt temperature prior to  
36 indentation. Median/radial cracking is observed for NABS-1 and NABS-2. On the other hand,  
37 the ring and cone cracking response for NABS-4 is characteristic of anomalous glass. In  
38 between these two types of indentation cracking responses, a unique response is observed for  
39 NABS-3. At 1 kgf, a semicircular crack is observed on the bottom half of the indent that is just  
40 outside of the radial cracks. At 2 kgf, this circular crack again forms and completely surrounds



1 the indent impression and radial cracks. Since this circular crack blocks the extension of radial  
2 cracks, it is referred to as a “boundary forming annular crack”. Boundary forming annular crack  
3 formation occurs after the full unloading cycle, so it is driven by residual stress. The magnitude  
4 of residual stress depends on the amount of deformed volume, so it is then expected that a  
5 residual stress-driven cracking system will be more developed at higher indentation loads. Since  
6 the annular crack was partially formed for NABS-3 at 1 kgf as shown in Fig. 3c, the effect of  
7 minor structural changes on cracking behavior was examined by changing the fictive  
8 temperature. As shown in Fig. 4, the more compact structure with a lower fictive temperature,  
9 i.e.,  $T_f = \text{strain pt.} = 501^\circ\text{C}$ , moves towards normal cracking behavior, whereas the more open  
10 structure with a higher fictive temperature, i.e.,  $T_f = 10^{10} \text{ Pa s} = 620^\circ\text{C}$ , moves towards  
11 anomalous behavior and more pronounced annular cracking. The impact of fictive temperature  
12 on refractive index and density is shown in Fig. 5 for NABS-3. The thin 1.0 mm refractive index  
13 parts were suitable for setting the fictive temperature above the anneal pt. since they could be  
14 rapidly cooled without thermal shock cracking. Challenges with rapid cooling of the thick  
15 density samples prevented proper resetting of the fictive temperature above the anneal pt.  
16 Therefore, the refractive index was measured at all three fictive temperatures, while density was  
17 only measured at the anneal and strain points where relaxation times are considerably longer and  
18 slower cooling is adequate. As shown in Fig. 5, the refractive index and density both decrease  
19 with increasing fictive temperature as expected. The linear change in index in this fictive  
20 temperature range gives confidence that the density change will also remain linear and the  
21 density at  $T_f = 620^\circ\text{C}$  is estimated to be  $2.267 \text{ g/cm}^3$  by the linear equation provided on the plot.  
22 The molar volume for glass at each fictive temperature is calculated by dividing the molecular  
23 weight by the density. The molar volumes for NBAS-3 at fictive temperatures of 501, 546, and  
24  $620^\circ\text{C}$  are 27.49, 27.51, and  $27.55 \text{ cm}^3/\text{mol}$ , respectively. The impact of fictive temperature on  
25 boron coordination is shown in Fig 2b for NABS-3. A slight increase in  $N_4$  is observed as fictive  
26 temperature is increased, with the shoulder at  $\sim -2 \text{ ppm}$  becoming more pronounced at higher  
27 fictive temperatures.

28 The initiation mechanism of the boundary forming annular crack was examined by cross-  
29 sectioning through the major diagonal of a 3 kgf Vickers indent in Fusion5® as shown in figure  
30 6b. The surface view of an indent in Fusion5 at 2 kgf is shown in Figure 6a and resembles the  
31 appearance of NBAS-3 in Fig. 3g. The cross-sectioned view shows that this glass forms a cone  
32 crack characteristic of anomalous glass such as silica on the loading half-cycle. Unexpectedly,  
33 the cone crack makes a  $\sim 90^\circ$  turn following unloading and is redirected back towards the surface  
34 to form the annular ring. Since cross-sectioning required many specimens/attempts to dissect the  
35 indent impression and capture the crack turning event, production Fusion5® glass was utilized.  
36 In typical indents performed at 2 kgf the boundary forming annular crack intersects the surface  
37 every time, however, when conducting the cross-sectioning technique the redirected crack does  
38 not make it all the way to the surface. Further, we only see redirection on one side which  
39 happens to be the side opposite the starter crack. Indenting at the tip of starter crack, i.e., on a  
40 glass-to-glass interface, has a clear influence on the residual stress field as reported elsewhere<sup>31</sup>.

41 Fig. 7 shows the result captured by the in-situ retardance measurement system after unloading  
42 from a 3 kgf peak load Vickers indent in Fusion5® glass. Immediately after the indent a notable



1 stress concentration could be observed close to the plastic zone from which a lateral crack  
2 rapidly extended after  $\sim 750$  ms, the direction of crack growth coincided with the normal of the  
3 slow-axis (i.e., principle tensile stress axis), there was also notable residual stress around the  
4 cone crack which initiated during loading with tensile axes along the direction of the cone. The  
5 tip of the lateral crack settled into a position near the stress concentration at the tip of the cone  
6 crack, after  $\sim 8$  s stress appeared to be relieved at the coinciding crack tips where the crack front  
7 was redirected normal to the residual tensile stress axis of the cone crack (i.e., back towards the  
8 surface). The redirected crack slowly extended toward the surface over  $\sim 4$  s after its initiation.

9 Fig. 8. provides images of a 2 kgf Vickers indent in Fusion5®, both before and after thermal  
10 shock. Several of the radial cracks extend following thermal shock, but are shown to terminate  
11 at the boundary-forming annular crack. When the same indent & thermal shock test is  
12 conducted on soda-lime silicate in the same 50 mm x 50 mm x 1 mm part geometry, radial  
13 cracks extend from the indent to the edges of the specimen<sup>16</sup>.

14 To categorize the glasses along the deformation continuum between normal and anomalous  
15 glass, 30 mN Berkovich scratch pileup measurements were performed. As shown in previously  
16 published work on Berkovich scratch deformation, the amount of material displaced by volume-  
17 conserving shear can be quantified using AFM measurements<sup>9,32</sup>. Fig. 9 shows the AFM  
18 linescans for (a) anomalous silica glass, (b) intermediate CABS25, and (c) normal soda-lime  
19 silicate<sup>32</sup>. The percentages of the impression volumes displaced into the pileup regions were 9%,  
20 32%, and 50%, respectively. When we conduct the same analysis on the NABS series and  
21 Fusion5® glass, the space in between anomalous glass and our previously defined intermediate  
22 glass is interrogated. The NABS-1, NABS-2, and NABS-3 glasses had displaced volumes of  $26 \pm 3\%$ ,  
23  $19 \pm 1\%$ , and  $10 \pm 3\%$ , respectively. An overlap of a characteristic linescan for each  
24 NABS glass is shown in Fig. 10. The cleaning procedure used to ensure high resolution AFM  
25 measurements resulted in pitting in NABS-4, so the pile-up measurement is not included.  
26 Fusion5® glass was also measured and had a displaced volume of  $15 \pm 1\%$  as shown in Figure  
27 11. A visual representation of where the NABS glasses and Fusion5® reside on the deformation  
28 continuum is provided in Figure 12. NABS-3 and Fusion5® are labeled (BF) in the figure for  
29 their ability to form boundary forming annular cracks by Vickers indentation in specimens with  
30 fictive temperature set to the anneal pt. temperature. These glasses are near the anomalous end  
31 of the spectrum, but with slightly more volume conserving shear deformation than silica.  
32 NABS-1 and NABS-2 are labeled (I) as additions to the previously defined intermediate space<sup>9</sup>.  
33 Like the intermediate CABS glasses described previously, they have significantly greater shear  
34 than anomalous silica and significantly greater densification than normal soda-lime silicate<sup>9</sup>. As  
35 with other intermediate glasses, NABS-1 and NABS-2 are advantageous for median/radial crack  
36 resistance and deform with enough shear to prevent ring and cone cracking<sup>9</sup>. The intermediate  
37 NABS-1 and NABS-2 have median/radial cracking threshold of 0.5-1.0 kgf. The pile-up  
38 volumes were also measured for NABS-3 at the three fictive temperatures studied. The results  
39 were  $10.8 \pm 0.6\%$ ,  $9.7 \pm 2.7\%$ , and  $9.5 \pm 1.3\%$ , for fictive temperatures of 501, 546, and 620°C,  
40 respectively.

## 41 Discussion



1 In this study, a glass series was designed that shows the transition in indentation behavior from  
2 glass that deforms with an intermediate amount of shear (median/radial crack forming) to highly  
3 densifiable, anomalous glass (ring/cone crack forming). The series passes through a  
4 composition, NBAS-3, that demonstrates boundary forming annular cracking. The images in  
5 Fig. 3, particularly in images e-h, show this transition clearly. The relative contributions to  
6 deformation from densification and shear allow us to better characterize these glasses and  
7 understand our observations. In previous work, the amount of volume displaced via shear into  
8 the pileup region for 30 mN Berkovich scratches was measured by AFM line scans for various  
9 glass types as shown in Fig. 9. The three glass categories, i.e., normal, intermediate, and  
10 anomalous, provide points of reference on the scale of the deformation continuum shown in Fig.  
11 12. The region between the previously defined intermediate glasses (26-32% displaced volume)  
12 and anomalous glasses (9% displaced volume) was targeted when designing the NABS glass  
13 series to seek the location of glasses that display the boundary forming annular crack. The  
14 displaced volume measurements of NABS-1, NABS-2, and NABS-3 are given in Fig. 10 and  
15 cover the desired range with values of 26, 19, and 10%, respectively. As shown in Fig. 11, the  
16 Fusion5® production glass has a displaced volume of 15%, also falling within our target range of  
17 exploration. When looking again at the deformation continuum scale in Fig. 12, it is shown that  
18 the boundary forming crack appears at displaced volumes of 10 and 15% for NABS-3 and  
19 Fusion5® glasses, respectively. The location near the anomalous end of the scale is critical so  
20 that the surface tensile stress surrounding the indenter during loading is high enough that a ring  
21 crack forms at the periphery of the indent and extends into the subsurface to make a classic cone  
22 crack<sup>12</sup>. This is shown as the crack that formed during the loading cycle in Fig 6b. Following  
23 unloading, the unexpected redirection of the crack towards the surface to create the boundary  
24 forming annular crack is observed. The formation of the large annular crack often takes several  
25 minutes to form following unloading as the residual stress drives this crack back towards the  
26 surface. It is typical that a semi-circle will form first, then the complete annular crack forms as  
27 semi-circle extends on a path around the indent. In typical anomalous glasses like silica, this  
28 crack redirection is not observed. We also do not see it in the most anomalous glass of our  
29 series, NABS-4. The residual stress that drives the boundary forming crack back to the surface is  
30 unique to glasses like NABS-3 and Fusion5® that have greater shear than typical anomalous  
31 glasses as shown in Fig. 12. While NABS-3 has only slightly higher overall displaced volume  
32 than silica, the visual comparison from Fig. 9a and 10 shows noticeable pile-up for NABS-3 that  
33 is not present for silica. The 3% error bars for the measurements for both NABS-3 and silica  
34 may lead to the unexpectedly similar % displaced volume. With replicate measurements at the  
35 various fictive temperatures for NABS-3 all providing values near 10%, the emphasis of future  
36 work will be to reduce the error on measurements made on silica. The value of 15% +/- 1%  
37 displaced volume for the near perfect surface on the fusion produced Fusion5® can be taken with  
38 higher confidence to define a position on the continuum that produces a boundary-forming  
39 annular crack. The positions of the NAB-3 and Fusion5® glasses on the deformation continuum  
40 suggest a unique combination of deformation by shear and densification modes. Cone crack  
41 redirection back to the surface may be explained by considering the residual stress contribution  
42 from the greater shear contribution for these glasses<sup>12</sup>. In glasses that deform with more shear,  
43 the residual stress field that drives lateral cracks is significantly higher than in anomalous



1 glasses<sup>12-13</sup>. Typically, lateral cracks originate at the bottom of the deformation zone boundary  
2 and initially propagate outward in the direction parallel to the glass surface after unloading. At  
3 some distance away from the indent, the lateral cracks can turn upward to intersect the surface  
4 and create chips<sup>8</sup>. As shown in Fig. 6b, traditional lateral cracks form in Fusion5® in the typical  
5 location at the bottom of the deformation zone and extend outward until they meet the cone crack  
6 boundary. While the lateral cracking system terminates at the cone crack boundary, the residual  
7 stress field is still present. Fig. 7 shows a time series of retardance measurements taken through  
8 the cross-section of Fusion5®. The lateral crack again terminates on this side of the cone crack,  
9 but the lateral crack-driving residual stress field moves towards the tip of the cone crack, then  
10 wraps around it in a manner that drives it back to the surface. In previous work by Tandon et al.,  
11 a cracking system that appears to be a boundary-forming annular crack was shown<sup>33</sup>. This  
12 cracking system was described as an interaction between a lateral crack and a cone crack, similar  
13 to the current work. Since the NABS-1 and NABS-2 have characteristics of intermediate glass,  
14 they are labeled as such in Fig. 12 and provide an expansion to this previously defined space.

15 The region of the deformation continuum that produces the boundary forming annular crack is  
16 now defined in Fig. 12, but the formation of this crack is dependent on the indentation load. At 2  
17 and 3 kgf, the annular crack readily forms, but at 1 kgf, it only partially forms as shown for  
18 NABS-3 in Fig. 3c. The partially formed crack provides the opportunity to study the impact of  
19 fictive temperature on cracking. For the sample treated to set the fictive temperature to the strain  
20 pt, the molar volume is the lowest at 27.49 cm<sup>3</sup>/mol indicating the highest packed structure of the  
21 three fictive temperatures studied. In turn, the displaced volume is also the highest at 10.8%.  
22 Surprisingly, this slight move along the scale towards normal glass results in the suppression of  
23 the initial ring crack and normal median/radial cracking is observed. By setting the fictive  
24 temperature to the anneal pt (the standard condition for our study), the molar volume increases to  
25 27.51 cm<sup>3</sup>/mol and the displaced volume is reduced slightly to 9.7%. As previously mentioned,  
26 this condition shows the partially developed annular crack. At the highest fictive temperature,  
27 620°C, the molar volume is highest at 27.55 cm<sup>3</sup>/mol, the displaced volume is reduced again to  
28 9.5%, and a fully developed annular crack is observed. High fictive temperature and the  
29 associated open network is more prone to densification, thus increasing the ring crack forming  
30 stresses at the periphery of the indent and the stresses that drive formation of the initial cone  
31 crack. A well-developed cone crack is a necessary pre-requisite for the formation of the  
32 boundary forming annular crack as shown in Fig 6b. At low indentation loads, e.g. 1 kgf, this is  
33 more challenging and apparently requires the boost provided by a more open, more anomalous,  
34 and thus more densifiable structure. Another interesting finding from the fictive temperature  
35 study is that the lower fictive temperatures show more B-O-B bonds and higher fictive  
36 temperatures show more B-O-Si bonds among the tetrahedrally coordination boron (peak at -2  
37 ppm). This may suggest that a very fine scale phase separation is taking place at lower fictive  
38 temperatures with a boron-rich phase forming. This is not obvious to the naked eye and the most  
39 obvious change is in the NABS-3 specimen with  $T_f = \text{strain pt}$ . While this thermal history is of  
40 the least practical interest since it requires arduous thermal treatment, it may also have some  
41 impact on the indentation deformation behavior and the transition to normal cracking. The  
42 hypothesis of fine scale phase separation at lower fictive temperatures is further supported by the  
43 unexpected, but minor increases in the fraction of  $N_4$  as fictive temperature is increased. This



1 also supports the hypothesis that boron is segregating a lower fictive temperature. Transmission  
2 electron microscopy will be conducted in future work to confirm or refute this explanation.

3 The subset of glasses that form the boundary forming annular crack offer a unique solution to  
4 maximize damage resistance. The annular crack provides a boundary that blocks the extension  
5 of radial cracks, even following thermal shock events as shown in Fig. 8. This material,  
6 commercialized as Corning® Fusion5®, found an initial application as a crack-resistant  
7 automotive windshield glass. Since Vickers contact so closely replicates the rock strikes that  
8 cause windshield breakage, this solution was found to be ideal<sup>16,17</sup>.

9

## 10 **Conclusion**

11 The characterization of glasses as normal or anomalous regarding indentation response is  
12 adequate for extreme endpoint glasses such as soda-lime and silica. Most current technical  
13 silicate glasses fall somewhere between these two endpoints with less shear than soda-lime and  
14 less densification than silica. By considering the indentation response as a continuum, we can  
15 target and explore unique combinations of deformation modes. Previously, so-called  
16 intermediate glasses were examined that were directly between soda-lime and silica in the  
17 proportions of shear and densification. In intermediate space, highly crack resistant glasses were  
18 discovered that dissipated the indentation energy through highly delocalized, fault-free shearing.  
19 Another mechanically advantaged space is identified in this current study near the anomalous  
20 end of the deformation continuum, but having more volume-conserving shear than fully  
21 anomalous glasses like silica. The anomalous densification contribution ensures a driving force  
22 for typical cone cracking, while the shearing contribution provides the residual stress that drives  
23 the cone crack back to the surface to create the boundary forming annular crack. The name  
24 “boundary forming annular crack” was coined since it prevents radial crack extension, even  
25 during extreme thermal shock events. Combining the modes of deformation in various  
26 proportions through careful glass design enables us to tailor indentation responses and invent  
27 new and highly damage resistant materials. The plot shared here for the deformation continuum  
28 highlights some of the novel indentation responses found thus far, but open space remains that is  
29 ripe for exploration.

30

31

32

33

34

35

36

37



1 **REFERENCES**

- 2 1 J.E. Neely and J.D. Mackenzie, *J. Materials Sci.*, 1968, **3**, 603, DOI:10.1007/BF00757906.
- 3 2 K.W. Peter, *J. Non-Cryst. Solids*, 1970, **5**, 103, DOI:10.1016/0022-3093(70)90188-2.
- 4 3 F.N. Ernsberger, *J. Non-Cryst. Solids*, 1977, **25**, 293.
- 5 4 J.T. Hagan and M.V. Swain, *J. Phys. D: Appl. Phys.*, 1978, **11**, 2091.
- 6 5 A. Arora, D.B. Marshall, B.R. Lawn, M.V. Swain, *J. Non-Cryst. Solids*, 1979, **31**, 415.
- 7 6 J.T. Hagan, *J. Mater. Sci.*, 1979, **14**, 462.
- 8 7 J.T. Hagan, *J. Mater. Sci.*, 1980, **15**, 1417.
- 9 8 R.F Cook and G.M. Pharr, *J. Am. Ceram. Soc.*, 1990, **73**, 787, DOI:10.1111/j.1151-  
10 2916.1990.tb05119.x
- 11 9 T.M Gross, J.Wu, D.E. Baker, J.J. Price, R. Yongsunthon, *J. Non-Cryst. Solids*, 2018, **494**, 13,  
12 DOI:10.1016/j.jnoncrsol.2018.04.048.
- 13 10 S. Yoshida, J-C. Sangleboeuf, T. Rouxel, *J. Mater. Res.*, 2005, **20**, 3404.
- 14 11 J.D. Mackenzie, *J. Am. Ceram. Soc.*, 1963, **46**, 461.
- 15 12 E.H. Yoffe, *Philos. Mag. A*, 1982, **16**, 617.
- 16 13 T.M. Gross, *J. Non-Cryst. Solids*, 2012, **358**, 3445.
- 17 14 S. Bista, J.F. Stebbins, J. Wu, T.M. Gross, *J. Non-Cryst. Solids*, 2017, **478**, 50.
- 18 15 J. Wu, T.M. Gross, L. Huang, S.P. Jaccani, R.E. Youngman, S.J. Rzoska, M. Bockowski, S. Bista, J.F.  
19 Stebbins, M.M. Smedskjaer. *J. Non-Cryst. Solids*, 2020, **530**, 119797.
- 20 16 T.M. Cleary, T.M. Gross, J. Wu, United States Patent 11,951,713, April 9, 2024.
- 21 17 T.M. Cleary, T.M. Gross, J. Wu, United States Patent 12,122,714, October 22, 2024.
- 22 18 ASTM International, ASTM C693-93, 2019.
- 23 19 ASTM International, ASTM E228-22, 2023.
- 24 20 ASTM International, ASTM C1350-96, 2019.
- 25 21 ASTM International, ASTM C1351M-96, 2022.
- 26 22 ASTM International, ASTM C623-21, 2021.
- 27 23 ASTM International, ASTM C1648-12, 2018.
- 28 24 T.M. Gross and R. Youngman, In: *Flexible Glass: Enabling Thin, Lightweight, and Flexible*  
29 *Electronics*, S. Garner (Ed.), Wiley, New York, (2017) 63-83.
- 30 25 D. Massiot, F. Fayon, M. Capron, I. King, S. Le Calve, B. Alonso, J.O. Durand, B. Bujoli, Z. Gan, G.  
31 Hoatson, *Magn. Reason. Chem.*, 2002, **40**, 70.
- 32 26 D.R. Neuville, L. Cormier, D. Massiot, *Geochim. Cosmochim. Acta*, 2004, **68**, 5071.



- 1 27 L.-S. Du, J.F. Stebbins, *J. Non-Cryst. Solids*, 2003, **315**, 239.
- 2 28 H. Aben and C. Guilleminot, *Photoelasticity of glass*, Springer-Verlag, Berlin (1993).
- 3 29 H. Yamashita, H. Yashino, K. Nagata, H. Inoue, T. Nakajin, T. Maskawa, *J. Non-Cryst. Solids*, 2000,
- 4 **270**, 48. DOI: 10/1016/S0022-3093(00)0056-9.
- 5 30 L.-S. Du, J.F. Stebbins, *J. Phys. Chem. B*, 2003, **107**, 10063.
- 6 31 Z.N. An, W.D. Li, F.X. Liu, P.L. Liaw, Y.F. Gao, *Metall. Mater. Trans. A* 2012, **43**, 2729. DOI:
- 7 10.1007/s11661-011-0992-5.
- 8 32 T.M. Gross, In: *The World Scientific Reference of Amorphous Materials: Structure, Properties,*
- 9 *Modeling, and Main Applications. Vol 2. -Structure, Properties, and Applications of Oxide Glasses*, P.C.
- 10 Taylor and I.E. Reimanis (Eds.), World Scientific, New Jersey (2021) 99-164.
- 11 33 R. Tandon, D.J. Green, R.F. Cook, *J. Am. Ceram. Soc.*, 1990, **73**, 2619.
- 12
- 13
- 14
- 15
- 16
- 17
- 18
- 19
- 20
- 21
- 22
- 23
- 24
- 25
- 26
- 27
- 28
- 29
- 30



1

Table I Compositions and Physical Properties of Lab Melted Glasses

Glass Code	NABS-1	NABS-2	NABS-3	NABS-4
<b>Batched composition (mol%)</b>				
SiO <sub>2</sub>	74	74	74	74
Al <sub>2</sub> O <sub>3</sub>	2	2	2	2
B <sub>2</sub> O <sub>3</sub>	6	11	16	21
Na <sub>2</sub> O	18	13	8	3
<b>Analyzed composition (mol%)</b>				
SiO <sub>2</sub>	77.18	78.97	76.42	75.54
Al <sub>2</sub> O <sub>3</sub>	1.98	2.04	2.04	2.01
B <sub>2</sub> O <sub>3</sub>	4.66	8.67	14.71	19.76
Na <sub>2</sub> O	16.14	10.28	6.8	2.66
minor constituents	0.04	0.04	0.03	0.03
Na <sub>2</sub> O - (Al <sub>2</sub> O <sub>3</sub> + B <sub>2</sub> O <sub>3</sub> )	9.50	-0.43	-9.95	-19.11
<b>Physical Properties</b>				
Density (g/cm <sup>3</sup> )	2.428	2.397	2.270	2.147
Coefficient of thermal expansion *10 <sup>-6</sup> (1/°C)	7.99	6.03	4.48	3.52
Strain Pt. (°C)	503	556	501	436
Anneal Pt. (°C)	542	596	546	491
Softening Pt. (°C)	720	770	755	781
10 <sup>10</sup> Pa s Temperature (°C)	605	659	620	586
Poisson's ratio	0.200	0.186	0.195	0.217
Young's modulus (GPa)	70.40	75.98	64.67	48.33
Shear modulus (GPa)	29.3	32.06	27.10	19.86

2

3

4

5

6

7

8

9

10

11

12

Table II Physical Properties of Fusion5®



<b>Glass ID</b>	<b>Fusion5®</b>
<b>R<sub>x</sub>O - (Al<sub>2</sub>O<sub>3</sub> + B<sub>2</sub>O<sub>3</sub>)</b>	-8
<b>Density (g/cm<sup>3</sup>)</b>	2.266
<b>Coefficient of thermal expansion *10<sup>-6</sup> (1/°C)</b>	4.66
<b>Strain Pt. (°C)</b>	496
<b>Anneal Pt. (°C)</b>	542
<b>Softening Pt. (°C)</b>	777
<b>Poisson's ratio</b>	0.190
<b>Young's modulus (GPa)</b>	63.70
<b>Shear modulus (GPa)</b>	26.50

1  
2  
3  
4  
5  
6  
7  
8  
9  
10  
11  
12  
13  
14  
15  
16  
17  
18  
19

Open Access Article. Published on 21 May 2026. Downloaded on 5/23/2026 10:25:03 AM.  
This article is licensed under a Creative Commons Attribution 3.0 Unported Licence.



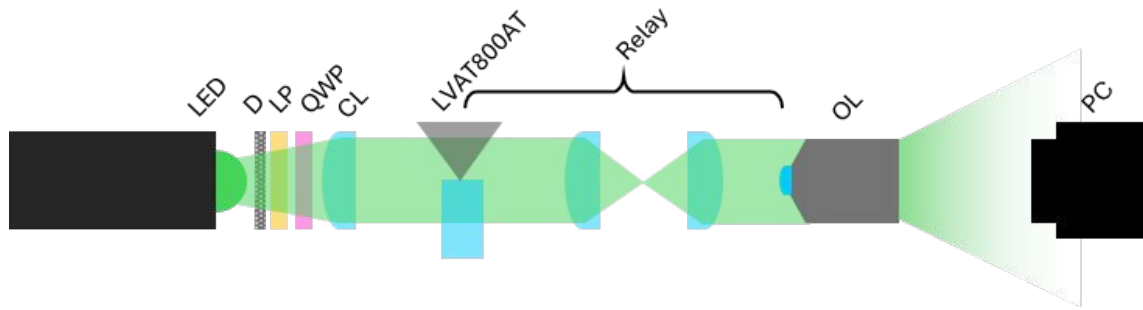
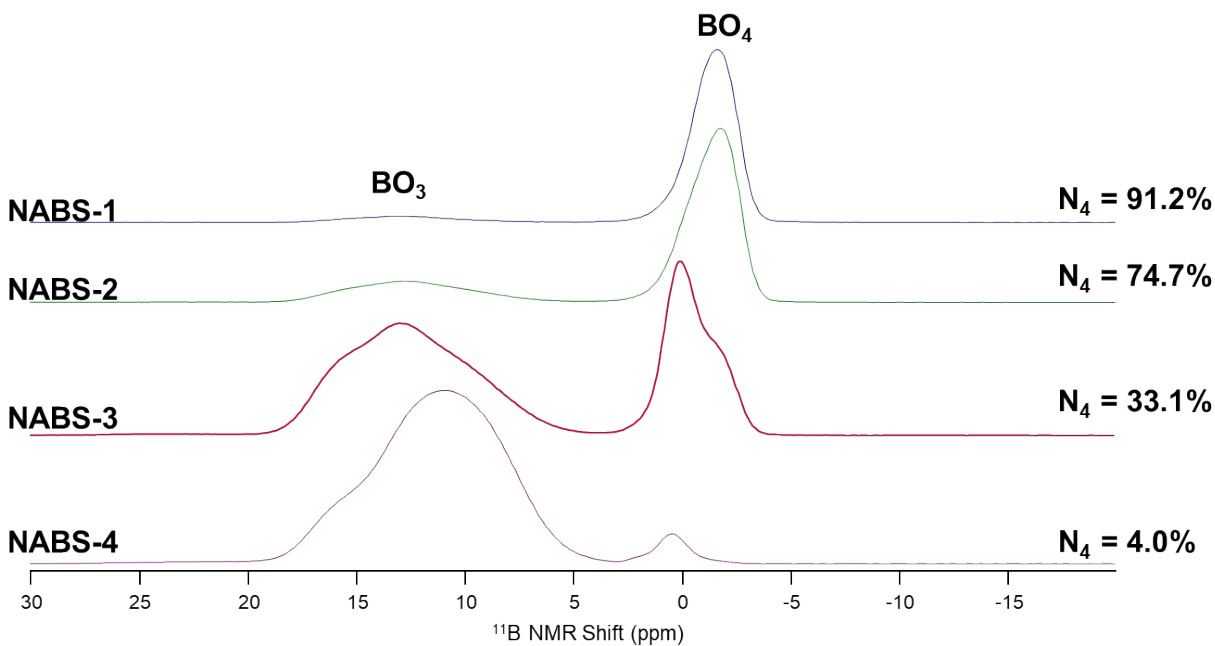


**FIGURE 1** Schematic of the in-situ photoelastic measurement system affixed to a LVAT800AT Vickers hardness tester.

1  
2  
3  
4  
5  
6  
7  
8  
9  
10  
11  
12  
13  
14  
15





1

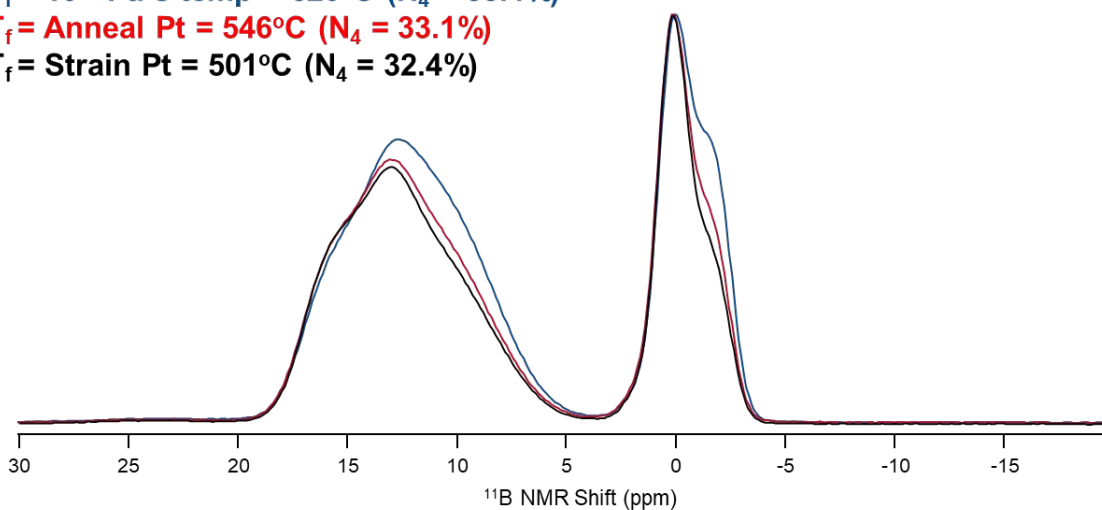
2

(a)

$T_f = 10^{10}$  Pa s temp = 620°C ( $N_4 = 33.4\%$ )

$T_f = \text{Anneal Pt} = 546^\circ\text{C}$  ( $N_4 = 33.1\%$ )

$T_f = \text{Strain Pt} = 501^\circ\text{C}$  ( $N_4 = 32.4\%$ )



3

4

(b)

5 **FIGURE 2 (a)  $^{11}\text{B}$  NMR on the NABS glass series with fictive temperatures set to the respective**

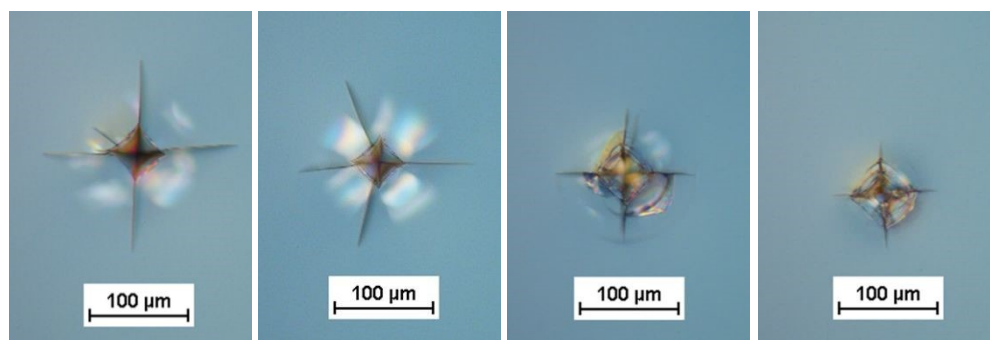
6 **anneal pt. temperatures (b)  $^{11}\text{B}$  NMR on NABS-3 at various fictive temperatures.**

7

8

9



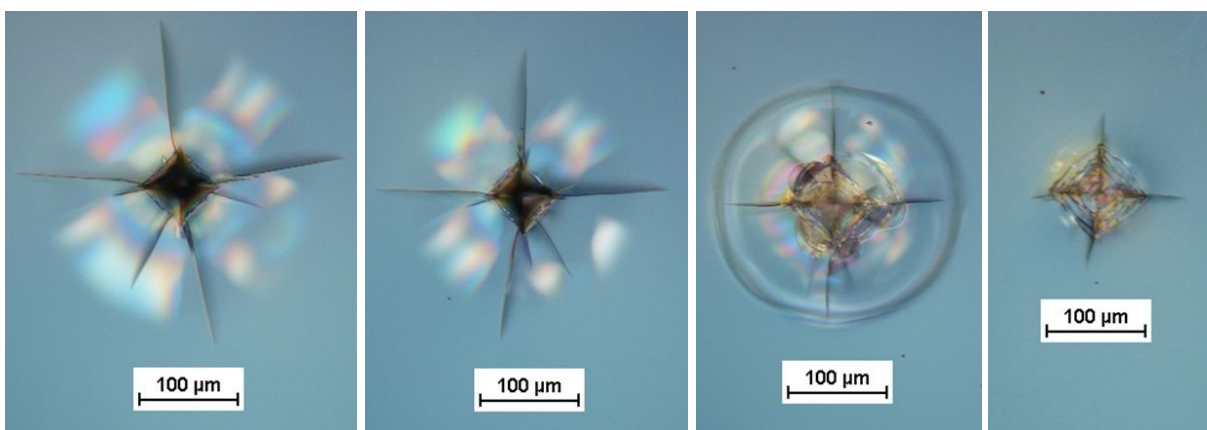


(a)

(b)

(c)

(d)



(e)

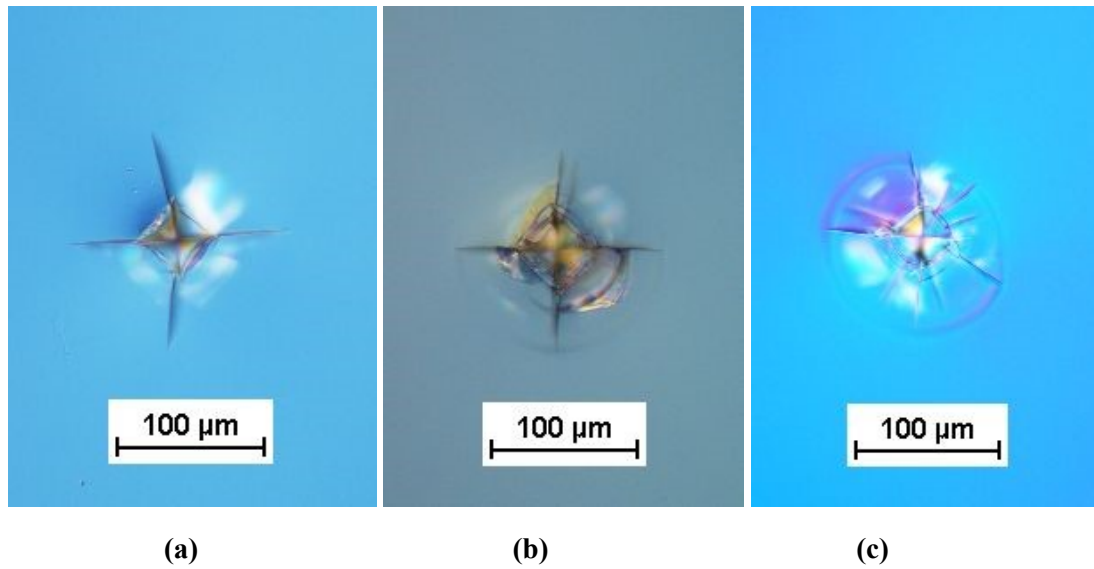
(f)

(g)

(h)

**FIGURE 3** Vickers indents at 1 kgf in (a) NABS-1, (b) NABS-2, (c) NABS-3, and (d) NABS-4. Vickers indents at 2 kgf in (e) NABS-1, (f) NABS-2, (g) NABS-3, and (h) NABS-4. Glasses were heat-treated to set the fictive temperatures equal to the respective anneal pt temperatures prior to indentation.





1  
2  
3 **FIGURE 4** Vickers indents at 1 kgf in NABS-3 at (a) fictive temperature = strain pt temperature,  
4 (b) fictive temperature = anneal pt temperature, (c) fictive temperature = temperature at  $10^{10}$  Pa s  
5 viscosity.



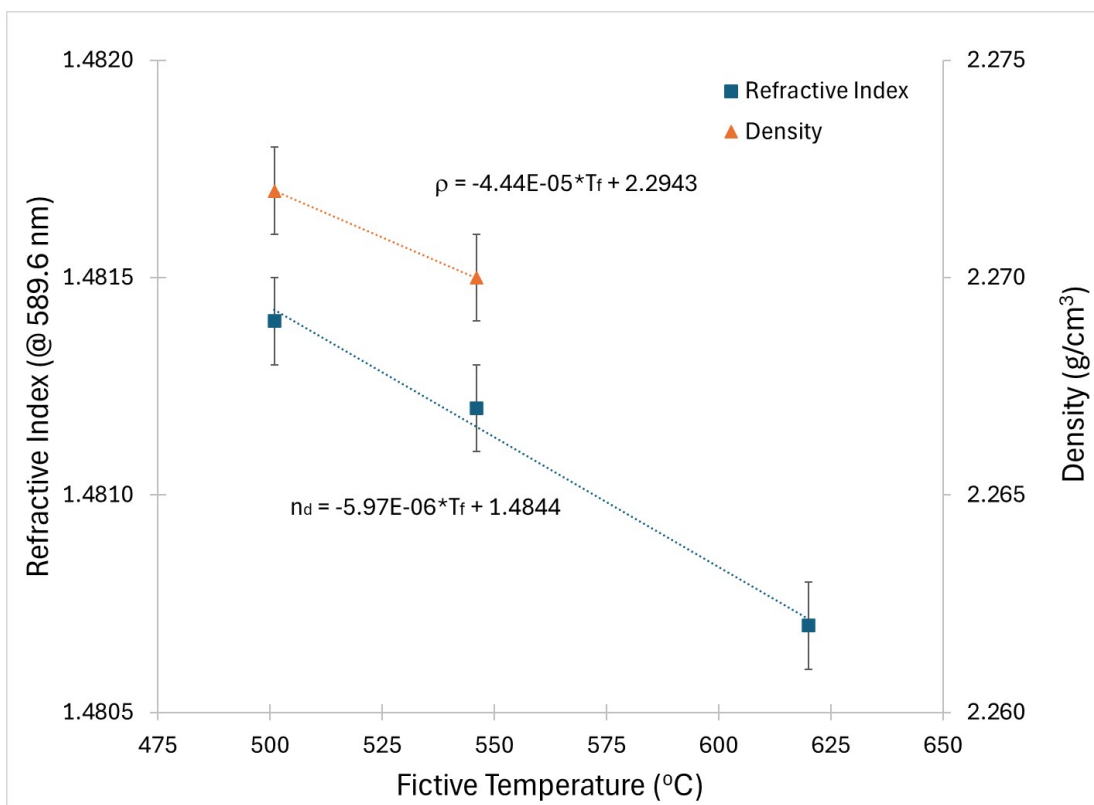
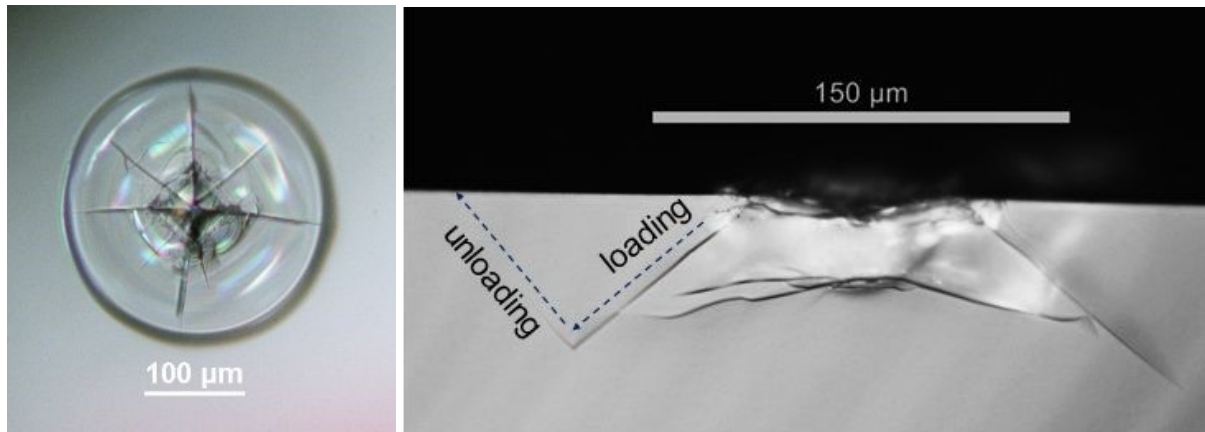


**FIGURE 5 Refractive Index and Density vs. Fictive Temperature for NABS-3**

1  
2  
3  
4  
5  
6  
7  
8  
9  
10  
11  
12  
13  
14  
15

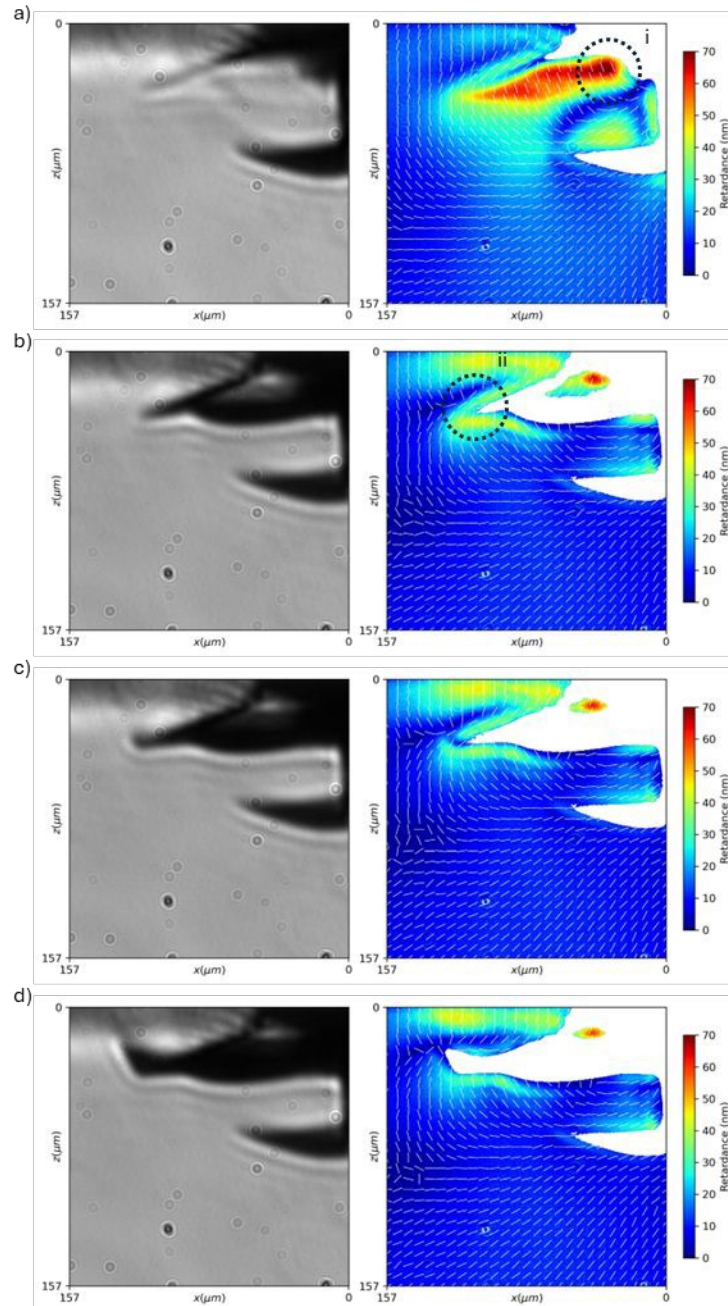




1  
2 **FIGURE 6 (a) Surface view of 2 kgf Vickers indent in Corning® Fusion5® with boundary forming**  
3 **annular crack. (b) Cross-sectional view of 3 kgf Vickers indent showing the cone crack that forms**  
4 **on the loading half cycle and the redirection of the cone crack to the surface on the unloading cycle.**

5  
6  
7  
8  
9  
10  
11  
12  
13  
14  
15  
16  
17  
18  
19  
20  
21  
22  
23





1  
2  
3 **Figure 7** Intensity (left) and retardance (right) images of crack systems formed after a 3 kgf  
4 Vickers indent on Fusion5 glass (subsamped slow-axis lines are overlaid on the  
5 retardance image). Images shown were taken a) immediately after unloading b) 750 ms  
6 after unloading c) 8 s after unloading d) 12 s after unloading. Regions of interest showing  
7 retardance concentrations before extension of i) lateral and ii) ring cracks.

8  
9



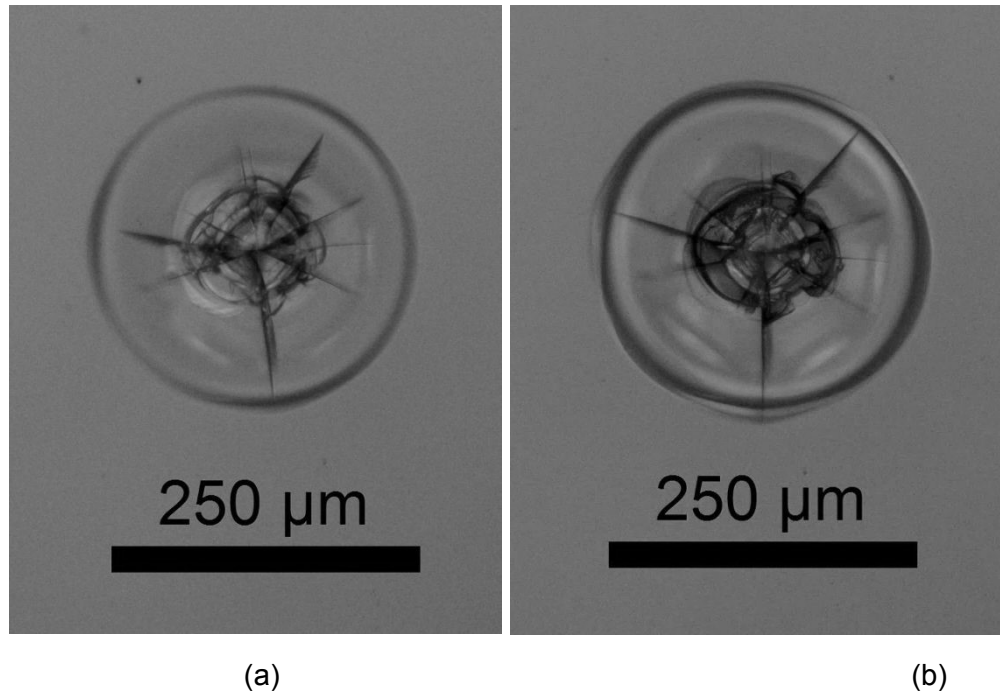
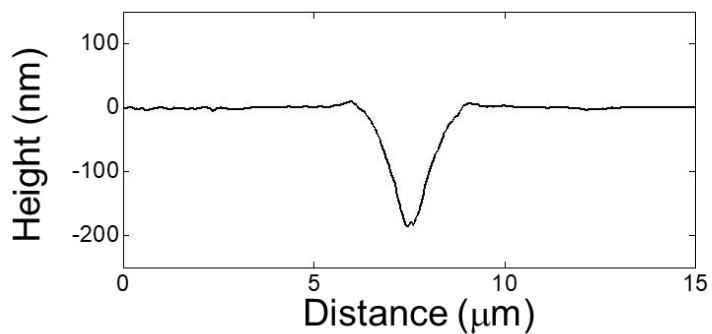


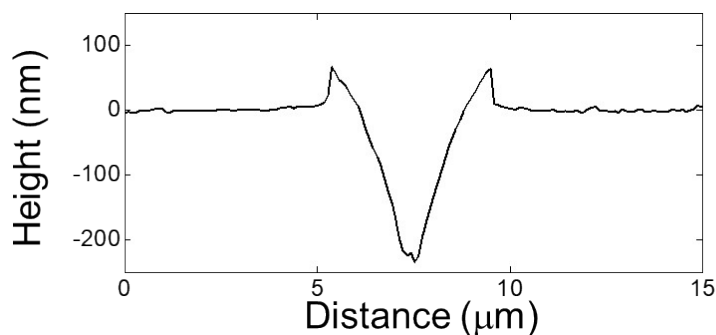
**FIGURE 8** (a) Image of indent in Fusion5® after 2 kgf indent. (b) Image of same indent after heating to 130°C and thermal shocking with ice water.

1  
2  
3  
4  
5  
6  
7  
8  
9  
10  
11  
12  
13  
14  
15  
16  
17  
18

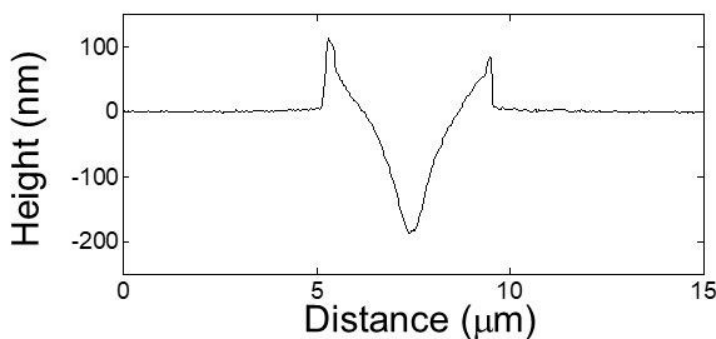




(a)



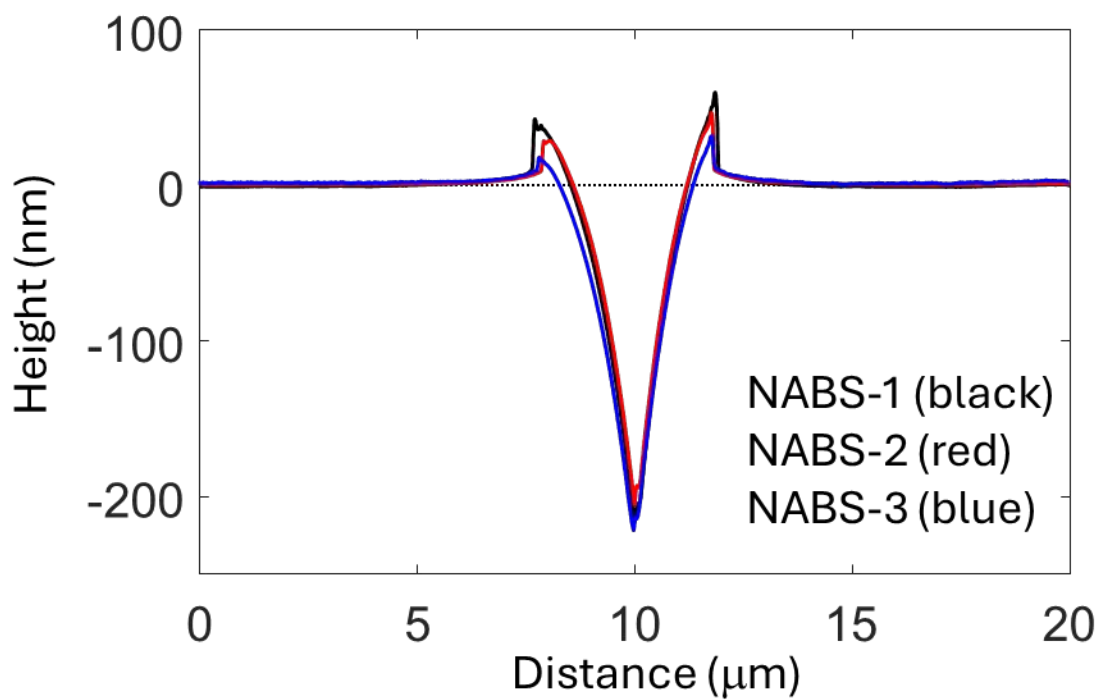
(b)



(c)

FIGURE 9 AFM scans across 30 mN Berkovich scratches in (a) anomalous silica glass, (b) intermediate CABS25 glass, and (c) normal soda-lime silicate glass. The percentage of material displaced into the pileup region is 9%, 32%, and 50% for these examples of anomalous, intermediate, and normal glass, respectively. Figure reproduced from Gross<sup>9</sup> following STM permissions guidelines.



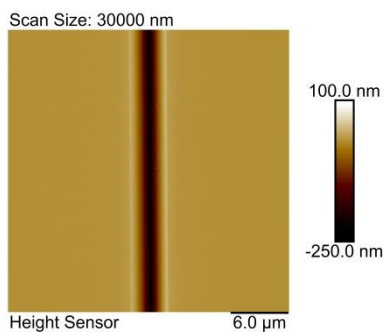
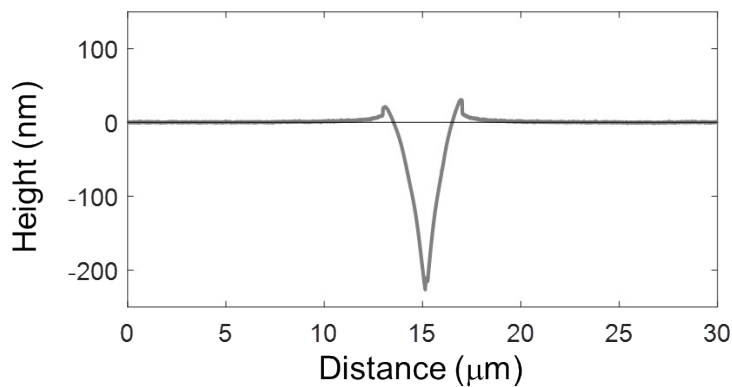


1  
2 **FIGURE 10** AFM line scan across a 30 mN Berkovich scratch in NABS series glasses. The  
3 percentage of material displaced into the pile-up regions is 26%, 19%, and 10% for NABS-1,  
4 NABS-2, and NABS-3, respectively.

Open Access Article. Published on 21 May 2026. Downloaded on 5/23/2026 10:25:03 AM.  
This article is licensed under a Creative Commons Attribution 3.0 Unported Licence.



5  
6  
7  
8  
9  
10  
11  
12  
13  
14  
15  
16



3  
4 **FIGURE 11 (a) AFM scan across a 30 mN Berkovich scratch in Fusion5® glass. The percentage of**  
5 **material displaced into the pile-up region is 15%. (b) AFM image of Berkovich scratch.**



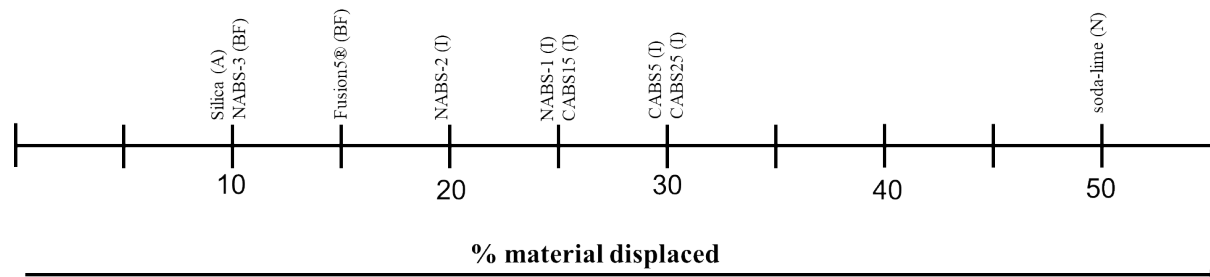


**FIGURE 12** Schematic representation of the indentation deformation continuum. Glasses are classified according to indentation deformation and cracking behavior by the amount of displaced material from Berkovich nanoscratch. Classifications are as follows: (N) normal, (I) intermediate, (A) anomalous, and (BF) boundary forming.



1  
2  
3  
4  
5  
6  
7  
8  
9  
10  
11  
12  
13  
14  
15  
16  
17  
18  
19  
20  
21  
22  
23  
24  
25  
26

1 **CRedit Contributor Statement**

2

3 **Fulmer, Brian D:** Investigation (Equal); Writing - Review & Editing (Equal).

4 **Gross, Timothy M:** Formal analysis (Equal); Investigation (Lead); Writing - Original Draft  
5 (Lead).

6 **Jones, Josh (S&T):** Formal analysis (Equal); Investigation (Equal); Writing - Review & Editing  
7 (Equal).

8 **Price, James J Dr:** Investigation (Equal).

9 **Singh, Keshaan:** Formal analysis (Equal); Investigation (Equal); Writing - Review & Editing  
10 (Equal).

11 **Wu, Jingshi:** Formal analysis (Equal); Investigation (Equal); Writing - Review & Editing (Equal).

12 **Yongsunthon, Ruchirej:** Formal analysis (Equal); Investigation (Equal); Writing - Review &  
13 Editing (Equal).

14 **Youngman, Randall E:** Formal analysis (Equal); Investigation (Equal); Writing - Review &  
15 Editing (Equal).

16



Additional data cannot be made available due to confidentiality requirements.

Open Access Article. Published on 21 May 2026. Downloaded on 5/23/2026 10:25:03 AM.  
This article is licensed under a Creative Commons Attribution 3.0 Unported Licence.

